

Photometric and Spectroscopic Analysis of V583 Lyrae, an Algol with a g -mode Pulsating Primary and Accretion Disk

HUI-TING ZHANG,^{1,2,3} SHENG-BANG QIAN^{①,2,3,*}, WEN-PING LIAO^{①,1,4}, B. SOONTHORNTHUM,⁵ AND N. SAROTSAKULCHAI⁵

¹Yunnan Observatories, Chinese Academy of Sciences (CAS), 396 yangfangwang, Guandu District, Kunming, 650216, P.R. China

²Department of Astronomy, School of Physics and Astronomy, Yunnan University, Kunming 650091, P. R. China

³Key Laboratory of Astroparticle Physics of Yunnan Province, Yunnan University, Kunming 650091, P. R. China

⁴University of Chinese Academy of Sciences, No.1 Yangqihu East Rd, Huairou District, Beijing, PR China, 101408

⁵National Astronomical Research Institute of Thailand (NARIT), 260 Don Kaew, Mae Rim Chiang Mai, Thailand, 50180

ABSTRACT

V583 Lyr is an extremely low mass ratio Algol-type binary with an orbital period of 11.2580 days. We determined an effective temperature of $T_{eff1} = 9000 \pm 350$ K from newly observed spectra, which might be an underestimate due to binary mass transfer. The binary mass ratio $q = 0.1 \pm 0.004$ and the orbital inclination $i = 85^\circ.5$ are determined based on the assumption that the secondary fills its Roche lobe and rotates synchronously. The radial velocity curve is obtained from time series spectra, allowing for improved estimation of stellar masses and radii: $M_1 = 3.56 \pm 0.5 M_\odot$, $R_1 = 2.4 \pm 0.2 R_\odot$; and $M_2 = 0.36 \pm 0.02 M_\odot$, $R_2 = 6.9 \pm 0.4 R_\odot$. The variations in the double-peaked H_α emission indicate the formation of a stable disk during mass transfer. V583 Lyr appears to be a post-mass-reversal system, according to the estimated mass transfer using O-C period analysis. Its orbital period is slowly increasing, from which the rate of mass accretion by the primary star is estimated to be $\dot{M}_1 = 3.384 \times 10^{-8} M_\odot \cdot yr^{-1}$. The pulsation analysis was conducted on the residuals of the light curve. The primary component was found to be a g -mode pulsating star with 26 frequencies extracted lower than $9 d^{-1}$. The frequency groups and rotational splitting properties of the g -mode were studied in detail. This study provides compelling evidence for an accretion disk surrounding the g -mode pulsating primary.

Keywords: binaries: eclipsing — binaries: spectroscopic — accretion disk — stars: pulsation

1. INTRODUCTION

The accretion structures formed are mainly determined by the relative separation of the components, the radius of the primary, and the mass ratio (Lubow & Shu 1975). In short-period Algols with $P \leq 4.5$ days, the gainer is larger and the gas stream from the inner Lagrangian point can impact the star directly. While if the gainer has a radius smaller than a certain specified size, relative to the binary separation, the infalling material has too much angular momentum for the stream to directly impact the gainer. The mass flow will miss the gainer and may collide with itself, changing its radial motion and instead feeding into a stable disk (Lubow & Shu 1975). This behavior usually occurs in long-period systems ($P \geq 6$ d). And there remains the case of a gainer with the radius between the minimum and disk radius, where a transient disk may exist. These are intermediate-period systems studied by Peters & Polidan (1998); Richards & Albright (1999) and references therein. An accretion disk may exist in β Lyrae-type (Mennickent 2022) and long-period Algol-type binary stars (Dervişoğlu et al. 2010). The disk precession (Doğan et al. 2015; Larwood et al. 1996) may cause periodic flux variations as the disk area projected in the direction of the observer's line of sight changes, which may be a compelling explanation for the long period variation in some double period variables (DPVs, e.g. AU Mon Lorenzi 1980; Djurašević et al. 2010)

V583 Lyr was recently analyzed by Zhang et al. (2020) and found to be a semi-detached binary with an extremely low mass ratio of ($q = M_2/M_1 = 0.096$). Gaulme & Guzik (2019) suggested that V583 Lyr may be the type of δ Sct or

* E-mail: qsb@ynao.ac.cn

tidal oscillations with frequencies larger than $5 d^{-1}$ and effective temperature (Baglin et al. 1973; Balona et al. 2015). However, they did not look for regular frequency spacing or any kind of pattern that would indicate a g -mode γ Dor star (Kaye et al. 1999; Van Reeth et al. 2016) or the slowly pulsating B (SPB, Waelkens 1991) stars. Zasche et al. (2015) found evidence supporting the possibility of a third body with a 50-year period, based on variations in previous photographic data. And Davenport (2016)’s statistical search for stellar flares reported 191 high levels of flare activity that are thought to be signals of light changes from binary eclipses.

V583 Lyr is an Algol system with an extremely low mass ratio and an orbital period of 11.2580 days. The strong double-peaked H_α emission is present in all observed spectra, one of the more prominent observational indicators of a permanent accretion disk. The mass transfer or accretion in V583 Lyr can be discovered from a detailed analysis of the available observations. Furthermore, V583 Lyr exhibits oscillations in all the photometric observations. We use the methods of asteroseismology, which involves the analysis of stellar pulsations to study stellar structure and evolution (Aerts et al. 2010), to provide a valuable supplement to the examination of V583 Lyr.

This paper presents the photometric and spectral observations and data reductions on V583 Lyr in section 2. From the spectroscopy study in section 3.1, the preliminary effective temperature of the hotter component is estimated. In section 3.2, the light curve synthesis was performed in conjunction with new data from *TESS* and a reanalysis of the *Kepler* data. To obtain the mass of the binary components, radial velocities are measured through spectroscopy in section 3.3. In section 3.4, we present a thorough spectroscopic analysis, highlighting the double-peaked H_α emission lines and the accretion disk. In section 3.5, we performed an asteroseismic analysis of the photometry for V583 Lyr, examining the frequency groups and g -mode splitting to determine the pulsation type and rotation of the gainer. Finally, in section 4, we provide the conclusions and discussions of our work.

2. OBSERVATION AND DATA REDUCTION

2.1. Photometric Data and Resampling

V583 Lyr was cataloged in *Kepler* Eclipsing Binary Stars (Prša et al. 2011) for photometric data by *Kepler* (Koch et al. 2010). The time series photometry data from *Kepler* between 2009 and 2013 for long-cadence (LC, 1800 seconds) light curves, and the short-cadence (SC, 60 seconds) data were observed for almost 3 cycles. Data are available at MAST ¹ in both SC and LC formats. We downloaded all available *TESS* (Transiting Exoplanet Survey Satellite) and *Kepler* observations of V583 Lyr using the `lightkurve` package (Lightkurve Collaboration et al. 2018). New observations from *TESS* were obtained in sectors 14, 40, 41, 53, and 54. The photometric band range for *TESS* (600-1000 nm) aiming for a photometric accuracy of 50 ppm on stars (Ricker et al. 2015). The *TESS* and *Kepler* data points are phase-folded and resampled using the method suggested by Zhang et al. (2020).

2.2. Spectroscopy data and reductions

The double-peaked H_α profile is observed by *LAMOST* (The Large Sky Area Multi-Object Fiber Spectroscopic Telescope, Luo et al. 2022) Low-Resolution Spectroscopic Survey (LRS) in June 2017, which suggests the presence of an accretion disk. So we conducted more optical spectroscopic observations of V583 Lyr at different eclipsing phases with Beijing Faint Object Spectrograph and Camera (*BFOSC*, Fan et al. 2016) of Xinglong 2.16 m telescope for direct imaging and low-resolution ($R \sim 500$ –2000) spectroscopy. Five spectra were obtained from February to May of 2023 with a spectral region of 387–676 nm. The *BFOSC* observations are listed in Table 1. All the observations and *LAMOST* LRS spectra (at phase of 0.66) cover the orbital circle roughly well. All spectra used in this work are normalized to the continuum approximated by spline functions, and the radial velocities (RVs) are heliocentric. The standard *IRAF* (the Image Reduction and Analysis Facility) routines were used to process the echelle spectroscopy data for flat and bias correction, wavelength calibration, and order merging. No flux calibration of the spectra was needed for our analysis.

¹ https://archive.stsci.edu/kepler/data_search/search.php

Table 1. Summary of new spectroscopic observations by *BFOSC*. The phases for these observations correspond to the ephemeris given in the *Kepler* Eclipsing Binary Catalog.

UT-date	Exptime(s)	BJD	Phase
2023-02-19	1800	2459995.369789	0.04906
2023-04-18	1800	2460053.255004	0.19080
2023-04-18	1800	2460053.275942	0.19266
2023-05-25	1800	2460090.183595	0.47104
2023-05-25	1800	2460090.204522	0.47289

3. ANALYSIS AND RESULTS

3.1. Temperature of the primary star

The effective temperature, 7500 ± 60 K, was given by calculating the average temperature of the two components from *LAMOST*. This is usually assigned to the primary star in the modeling procedure, T_{eff1} , which can be incorrectly estimated. Considering that the mixing of the binary components and the presence of H_α emission lines may affect the accuracy of the stellar atmospheric parameters, we try to determine the primary effective temperature by taking improved measures from the influence of the above two aspects. Based on the available spectroscopic data, V583 Lyr appears to be a single-line spectroscopic binary star. However, the lower resolution of the spectrum may be preventing us from distinguishing between the components of the system. Considering also that the mass ratio $q = \frac{M_2}{M_1}$ and the temperature ratio $\frac{T_2}{T_1}$ of the primary and secondary stars are small, we consider the primary’s contribution to be dominant. Therefore, we utilize the University of Lyon Spectroscopic Analysis Software (ULySS, Koleva et al. 2009) to derive the atmospheric parameters by minimizing the χ^2 value between the observed spectrum and a multidimensional grid of model spectra, which is constructed by interpolating the MILES library (Sánchez-Blázquez et al. 2006; Prugniel et al. 2011). The synthetic spectra were produced using a grid of Kurucz model atmospheres (Kurucz 1979) under Local Thermodynamic Equilibrium (LTE) conditions. The models have been calculated by means of a statistical distribution function representation of the opacity of almost 10^6 atomic lines.

This interpolator returns a spectrum for any temperature, metallicity, and gravity where each wavelength bin is calculated by interpolation over the entire reference library. It is constructed from three different sets of polynomials for the OBA, FGK, and M-type temperature ranges, and is linearly interpolated in overlapping regions. Each of these sets of polynomials is valid for a wide range of parameters, so it is a global interpolation.

The shape of stellar spectra is mainly influenced by T_{eff} , $\log g$, and $[Fe/H]$. To determine the T_{eff1} for V583 Lyr, the strong absorption lines that reliably trace T_{eff1} were ultimately selected. The fit is performed using Equation 3.1 over the wavelength range 4000-6500Å, where the H_α emission lines are rejected.

$$Obs(\lambda) = P_n \times G \otimes TGM(T_{eff}, \log g, [Fe/H], \lambda), \quad (3.1)$$

where $Obs(\lambda)$ is the observed one-dimensional spectral function of the wavelength (λ); P_n is a multiplicative polynomial of degree n ; G is a Gaussian broadening function; and TGM is a model spectrum as a function of T_{eff} , $\log g$, and $[Fe/H]$. The best-fitted results are shown in Figure 1, and the atmospheric parameters are listed in Table 2. There are 343 values for V585 Lyr in the *Gaia* DR3 BP/RP spectrum (Gaia Collaboration 2022) in a wide wavelength range from 336 to 1020 nm with 2 nm steps. The BP/RP spectrum of V583 Lyr estimated the effective temperature from the GSP-Phot Aeneas best library to be 9140.3 K, with lower (16%) and upper (84%) confidence limits of 8833.6 K and 9384.8 K, respectively. When dealing with A-type stars, it is important to consider the uncertainty in the effective temperature, which can be at least 100 K due to several factors, including continuum placement or spectrum normalization, uncertainties in microturbulence, and opacities used in the original model atmospheres. Therefore, based on the results listed in Table 2 and the *Gaia* DR3 BP/RP spectra, we have determined the mean temperature of T_{eff1} to be 9000 K with an estimated uncertainty of about 350 K.

3.2. Photometric analysis

In this section, we analyzed the new photometric data from *TESS* and reanalyzed the *Kepler* data for V583 Lyr. The Wilson-Devinney (W-D; Wilson & Devinney 1971; Wilson 1979, 1994) program was used with a detailed treatment

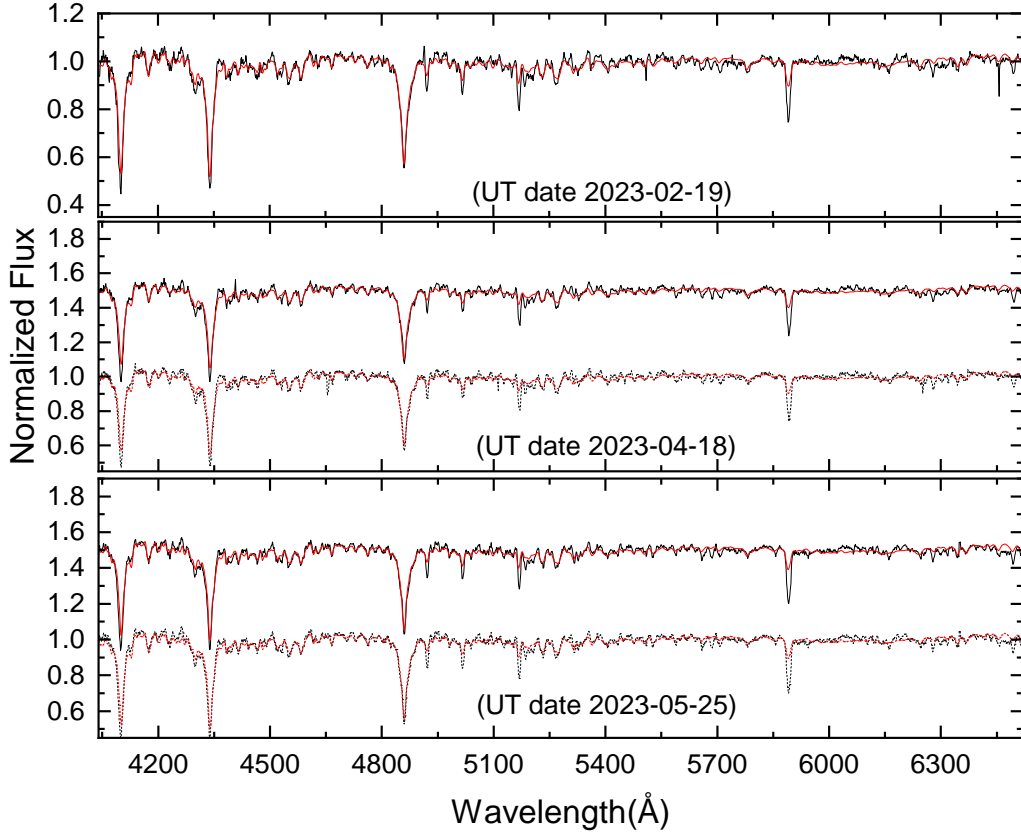


Figure 1. Spectrum fitting for V583 Lyr. Refer to Table 2 for the stellar parameters used for calculating the model spectrum.

Table 2. Derived atmospheric parameters for the V583 Lyr.

UT-date	Phase	T_{eff} (K)	$\log g$ (cms^{-2})	$[Fe/H]$ (dex)
2023-02-19	0.049	8970 ± 180	4.20 ± 0.1	0.35 ± 0.06
2023-04-18	0.191	8980 ± 200	4.04 ± 0.1	0.34 ± 0.06
2023-04-18	0.193	9000 ± 200	4.06 ± 0.1	0.33 ± 0.07
2023-05-25	0.471	8970 ± 160	4.24 ± 0.1	0.39 ± 0.05
2023-05-25	0.473	8970 ± 160	4.22 ± 0.1	0.37 ± 0.05

of limb darkening, gravitational darkening, and reflection effects to obtain a comprehensive set of stellar and orbital parameters. Using the ephemeris $BJD_0 = 55007.62275$ (Barycentric Julian Date-2400000) given in the *Kepler* Eclipsing Binary Catalog, we computed the phases and folded the light curve. The *TESS* and *Kepler* data were binned to 1000 and 600 points, respectively, for use in the binary modeling code.

Mode 5 (Semi-detached binary with the secondary star filled with its Roche Lobe) is chosen with a circular orbit (the orbital eccentricity $e = 0$). The adjustable orbital parameters include orbital inclination (i), the surface temperature of the secondary component (T_{eff2}), the dimensionless potential of the primary component (Ω_1), semi-major axis (a), phase shift (ϕ), luminosity of the primary component (L_1), and third light (l_3). And pass-band limb-darkening coefficients were from [van Hamme \(1993\)](#)'s table.

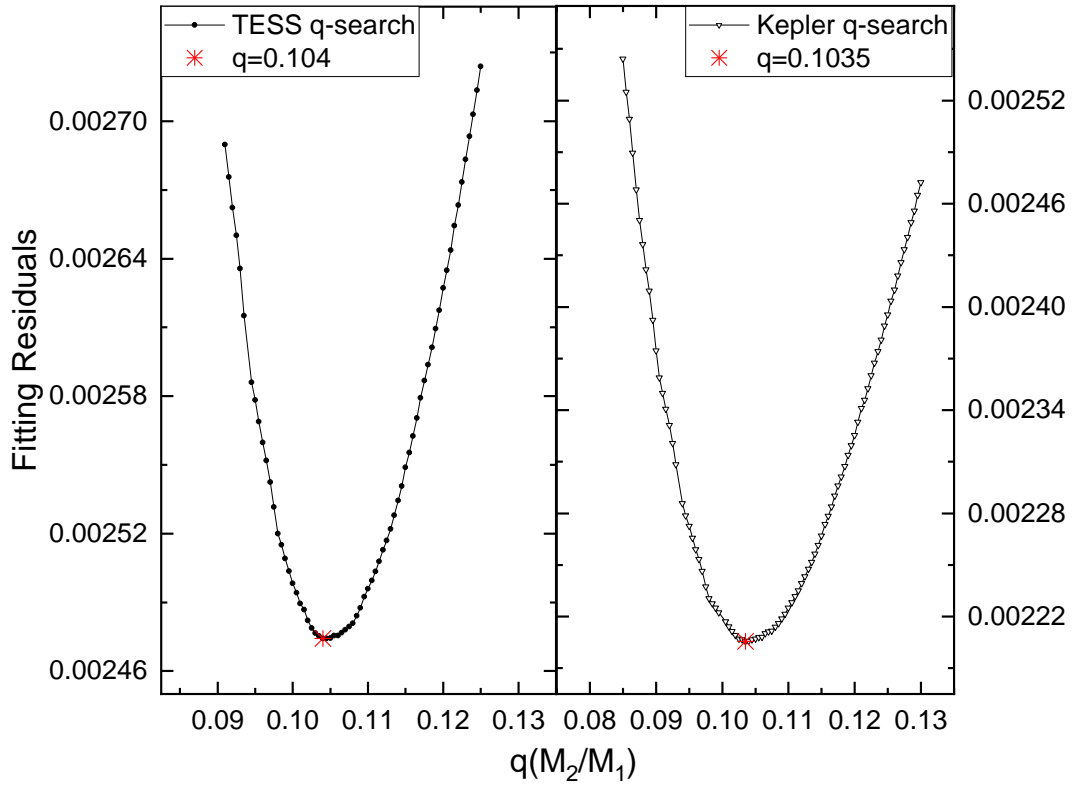


Figure 2. The results of the least squares minimization fit to estimate the initial value of the mass ratio q . The fitting residuals are plotted for $0.07 \leq q \leq 0.13$ with the step of 0.0005.

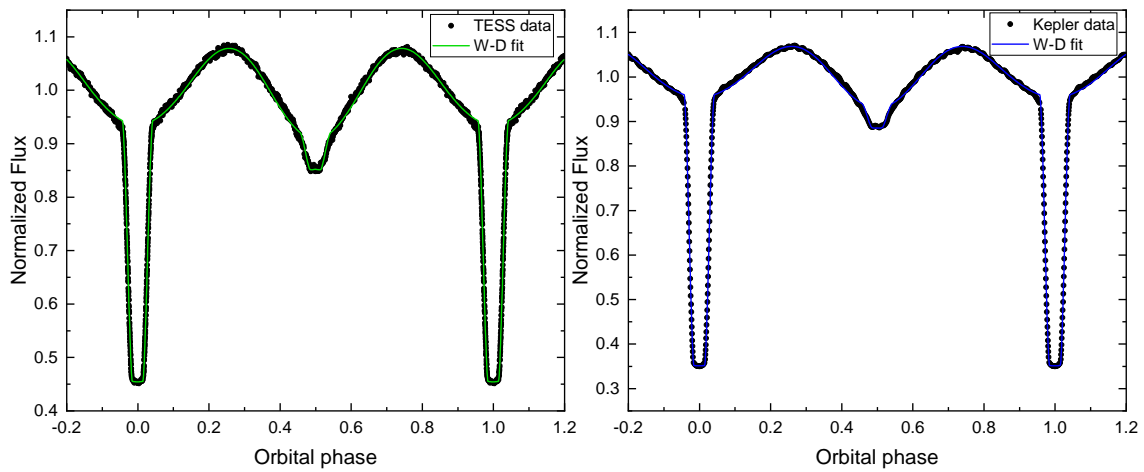


Figure 3. Theoretical binary model fit of *TESS* (left panel) and *Kepler* (right panel) in semi-detached mode.

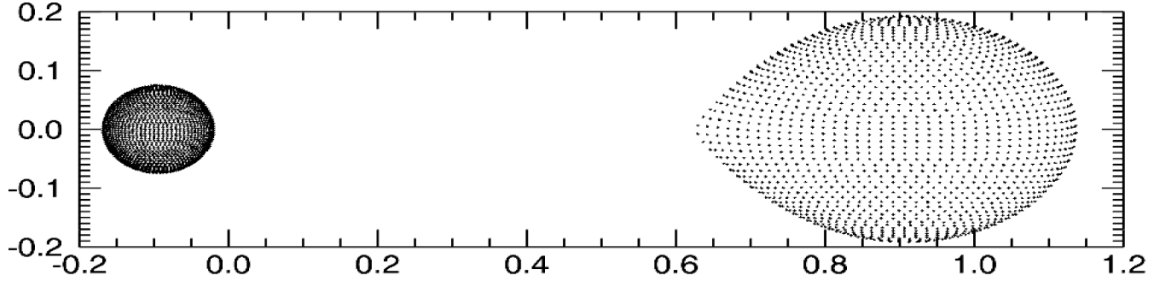


Figure 4. The semi-detached configuration of V583 Lyr in the phase = 0.25.

The primary effective temperature is fixed as $T_{eff1} = 9000 \pm 350$ K obtained in Section 3.1. We determined the mass ratio ($q = M_2/M_1$) by using the q-search² method with the step of 0.0005 in the range $0.07 \leq q \leq 0.13$. The results of the q-search are plotted in Figure 2 for *TESS* (left panel) and *Kepler* (right panel) photometry, which obtained the close search results of $q = 0.1035 \pm 0.0022$ and $q = 0.1040 \pm 0.0016$, and also close to the result of $q = 0.0962 \pm 0.0024$ obtained by Zhang et al. (2020). Based on the above results, we finally determine the best estimate for the mass ratio of V583 Lyr to be $q = 0.1 \pm 0.004$.

We then utilized both *TESS* and *Kepler* data for binary model fitting, yielding the orbital parameters and relative physical parameters listed in Table 3. The temperature ratio T_2/T_1 , relative radii r/a , orbital inclination i , and mean density $\rho_{1,2}$ obtained in our results generally align with those of Zhang et al. (2020), who solely analyzed *Kepler* data. The bolometric gravity darkening coefficient of the primary star (g_1) was set to 1.0 for radiative atmospheres from von Zeipel (1924), and the bolometric albedo value (A_1) was set to 1.0, from Ruciński (1969). While g_2 and A_2 of the secondary star are adjusted by the binary model because the detailed reflection effect and the Roche geometry of the evolved secondary star can be taken into account. We obtained the results $g_2 = 0.313 \pm 0.001$ and $A_2 = 0.715 \pm 0.006$ from *TESS* data and $g_2 = 0.298 \pm 0.003$ and $A_2 = 0.775 \pm 0.008$ from *Kepler* data. The final photometric solutions from *Kepler* and *TESS* photometry are listed in Table 3.

The luminosity ratio of $L_{1,2}/(L_1+L_2)$ varies between the *Kepler* and *TESS* bands. In the *Kepler* band, $L_1/(L_1+L_2)$ comprises approximately 58% while $L_2/(L_1+L_2)$ comprises roughly 42%. Conversely, in the *TESS* band, $L_1/(L_1+L_2)$ amounts to 46%, and $L_2/(L_1+L_2)$ amounts to 54%. This illustrates the secondary star’s superluminosity, potentially resulting from variances in photometric band ranges between *Kepler* and *TESS*. Finally, the light curves that resulted from the binary model’s fitting in both *Kepler* and *TESS* bands are displayed in Figures 3, and the semi-detached configuration is presented in Figure 4. Our results of the photometric analysis give the mean relative radius of the gainer as $R_1/a \approx 0.074$. It is below the ω_{min} curve based on the semi-analytical ballistic calculations of Lubow & Shu (1975), indicating the formation of a permanent disk (e.g., TT Hya, van Hamme & Wilson 1993; Miller et al. 2007).

3.3. Radial Velocities and Mass function

In this section, we attempt to measure radial velocities (RVs) to determine the fundamental properties of V583 Lyr. The heliocentric correction is done for *BFOSC* spectra using the IRAF `rvcorrect` task, and for *LAMOST* LRS spectra the vacuum wavelength has been converted to air wavelength using the refractive index of Ciddor (1996). The spectral lines of the secondary star are much sharper in our optical spectra than those of the primary star. This is because the lines of the primary are highly broadened by the star’s rotation and distorted by the presence of the accretion disk. Therefore, the lines of the secondary star are more accurate tracers of the orbital motion, resulting in more precise orbital elements compared to those derived from the lines of the primary.

The radial velocities were determined using the cross-correlation technique with an IRAF radial velocity package `xcsao` (Tonry & Davis 1979; Kurtz et al. 1992; Mink & Kurtz 1998). We selected a group of template spectra with known velocities from ELODIE library³ (Prugniel & Soubiran 2001), including three spectra from HD50692 (G0V, $v \sin i = 15$ km s⁻¹). The observed spectra were cross-correlated with the template spectrum to measure the radial velocities of the secondary star. The region near H_α was omitted during this process. The observations and the derived

² q-search is performed with the W-D program to search for the best fit mass ratio of the binary model in a given range of q values.

³ <http://atlas.obs-hp.fr/elodie/>

Table 3. The orbital and physical parameters resulting from the best-fitting binary model to *Kepler* and *TESS* photometry of V583 Lyr. The numbers in parentheses are the errors on the last bits of the data. $f_{1,2}$ represents the filling factors, which is the ratio of the stars’ volume to their Roche lobe volume (V_{star}/V_{RL}).

Parameters	<i>TESS</i>	<i>Kepler</i>
$P_{orb}(d)$	11.2580	11.2580
mode	semi-detached	semi-detached
$i(deg)$	85.456(21)	85.509(55)
$q = M_2/M_1$	0.104	0.1035
T_2/T_1	0.5416(9)	0.5316(18)
$L_1/(L_1 + L_2)$	0.4629(4)	0.5804(9)
$L_2/(L_1 + L_2)$	0.5371(4)	0.4196(9)
g_1	1.0(assumed)	1.0(assumed)
g_2	0.313(1)	0.298(3)
A_1	1.0(assumed)	1.0(assumed)
A_2	0.715(6)	0.775(8)
Ω_1	13.55(5)	13.82(14)
Ω_2	1.971(11)	1.970(6)
r_{pole1}/a	0.0743(3)	0.0730(8)
r_{pole2}/a	0.1921(12)	0.1918(6)
r_{point1}/a	0.0743(3)	0.0730(8)
r_{point2}/a	0.2856(12)	0.2852(6)
r_{side1}/a	0.0743(3)	0.0730(8)
r_{side2}/a	0.1997(12)	0.1994(6)
r_{back1}/a	0.0743(3)	0.0730(8)
r_{back2}/a	0.2307(12)	0.2305(6)
R_2/R_1	2.794(6)	2.707(21)
f_1	2.163(13)	2.033(34)
f_2	100.00(6)	100.00(5)
$\rho_1(\rho_\odot)$	0.2331(9)	0.2476(27)
$\rho_2(\rho_\odot)$	0.0011(2)	0.0011(1)

heliocentric radial velocities against the template are listed in Table 4. In Figure 5, the *RVs* are sorted by phase and fitted with a sine function through a Marquart-Levenberg method (Marquardt 1963):

$$RV = \gamma + K \sin [2\pi(\phi + \phi_0)] \quad (3.3)$$

A system velocity $\gamma = 53.7 \pm 3 \text{ km s}^{-1}$, the semi-amplitude of the secondary $K_2 = 135.5 \pm 6 \text{ km s}^{-1}$ and phase shift $\phi_0 = -0.68 \pm 0.01$ are estimated. The residuals from the RV-fitting function are indicated as O-C, listed in Table 4.

We calculated the mass function $f(m)$ defined for a single-lined spectroscopic binary as:

$$f(m) = \frac{M_1 \sin^3 i}{(1 + q)^2} = \frac{P_{orb}}{2\pi G} K_2^3, \quad (3.4)$$

where $P_{orb} = 11.2580 \text{ d}$ is the orbital period, the orbital inclination i and the mass ratio q_{phot} are the photometric solutions from Section 3.2. The mass of the primary star is calculated from Equation 3.4 as $M_1 = 3.56 \pm 0.5 M_\odot$, and $M_2 = M_1 \times q = 0.36 \pm 0.02 M_\odot$ is derived from the mass ratio $q \approx 0.1$. Then the semi-major axis is calculated using the third Kepler’s law:

$$\frac{a^3}{P^2} = \frac{G}{4\pi^2} (M_1 + M_2) \quad (3.5)$$

Table 4. Heliocentric radial velocities of the gainer obtained from the V583 Lyr spectra of *LAMOST* (2017) and *BFOSSC* (2023), and their respective errors, using the Gaussian function. Residuals from the RV-fitting function are indicated as O-C.

Phase	Velocity (km s ⁻¹)	error (km s ⁻¹)	O-C (km s ⁻¹)	Template spectra
0.049	-30.493	15.332	15.370	19951104-HD50692
0.049	-34.777	15.361	11.086	19971116-HD50692
0.049	-27.737	15.253	18.126	20011016-HD50692
0.191	48.408	19.188	-14.309	19951104-HD50692
0.191	45.327	19.100	-17.390	19971116-HD50692
0.191	52.896	18.920	-9.821	20011016-HD50692
0.193	60.376	18.964	-4.039	19951104-HD50692
0.193	56.948	18.879	-7.467	19971116-HD50692
0.193	63.216	18.967	-1.199	20011016-HD50692
0.471	191.938	21.432	7.111	19951104-HD50692
0.471	188.023	21.557	3.196	19971116-HD50692
0.471	194.004	21.543	9.177	20011016-HD50692
0.473	205.553	21.288	21.166	19951104-HD50692
0.473	202.264	21.294	17.877	19971116-HD50692
0.473	208.916	21.461	24.529	20011016-HD50692
0.663	57.669	10.241	-10.864	19951104-HD50692
0.663	54.141	10.362	-14.392	19971116-HD50692
0.663	61.271	10.308	-7.262	20011016-HD50692

Table 5. Absolute parameters of V583 Lyr compared to the results of [Zhang et al. \(2020\)](#).

Parameters	This work	Zhang et al. (2020)
T_{eff1} (K)	9000 ± 350	7484 ± 58
T_{eff2} (K)	4780 ± 100	4366 ± 57
M_1/M_\odot	3.56 ± 0.5	1.58 ± 0.49
M_2/M_\odot	0.36 ± 0.02	0.153 ± 0.051
R_1/R_\odot	2.4 ± 0.2	1.90 ± 0.28
R_2/R_\odot	6.9 ± 0.4	5.14 ± 0.79

to be $a = 33.34 \pm 0.18R_\odot$. The estimated absolute parameters are listed in Table 5 in comparison with the results of [Zhang et al. \(2020\)](#). They estimated the absolute physical characteristics of stars using the $\rho - T$ method (density-temperature method introduced in [Zhang et al. 2017](#)) in their study.

3.4. H_α profiles and accretion disk

The double-peaked emission is the most intriguing aspect of the H_α profile, which is mainly due to Thomson scattering of the light from the primary star. The accretion disk scatters light from the primary star, creating a wide emission line. This is superimposed on the absorption profile in the stellar atmosphere of the primary, resulting in the double peak emission profile. The broad wings of the emission profile extend from 6547 to 6574 Å. The variability

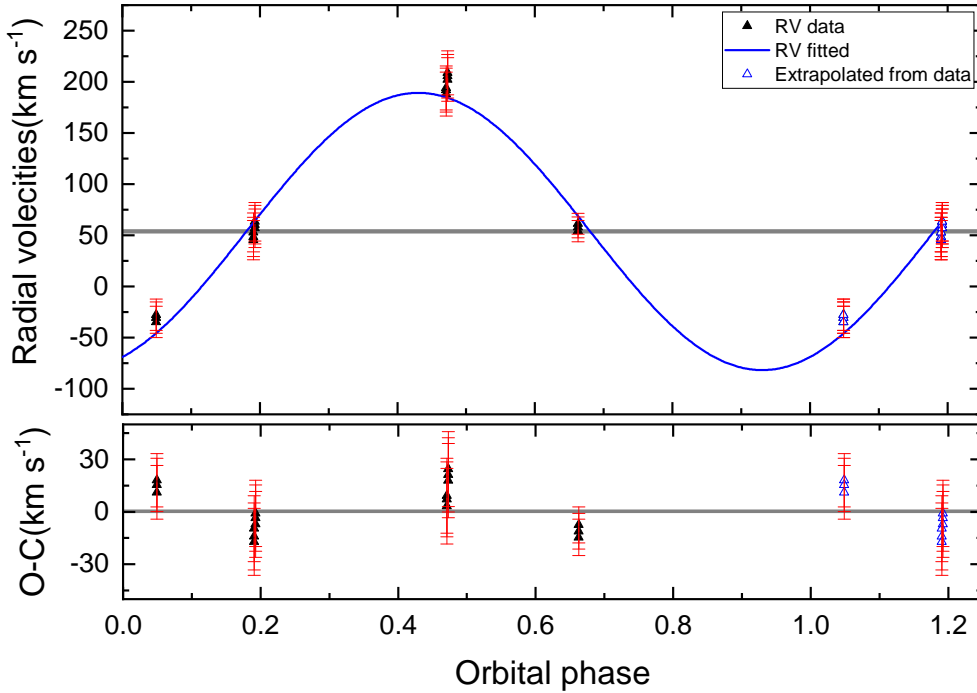


Figure 5. Upper panel: Velocity curve of V583 Lyr based on elements from Table 4 and the best-fitting solution. The horizontal dashed line marks the corresponding systemic velocity. Bottom panel: residuals from the fit.

of the H_α line profile with orbital phase is illustrated in Figure 6. The properties of H_α emission profile are listed in Table 6. From the currently available spectroscopic observations plotted in Figure 6, we can see the H_α blue-peak emission is larger than the red peak. The ratio B/R ⁴ of the H_α profile is calculated and listed in Table 6.

The variation of the center wavelength of the blue and red peaks with the orbital period is shown in Figure 7. The red peak shifts along with the central absorption line, and the average peak separation is $11.067 \pm 0.297 \text{ \AA}$. This value was used to determine the velocity of a particle located on the accretion disk rim, which is $V_{rim} = 253 \pm 10 \text{ km s}^{-1}$. The spectral data in Figure 6 and Table 6 show that the blue emission during the primary eclipse (phase = 0.049) is unexpectedly strong, while the red emission is comparatively weaker, as indicated by the double peaked emission intensities. The excess absorption in the core of H_α during these phases could be attributed to the eclipse effect, which suggests the possible presence of cooler circumstellar matter surrounding the secondary star. Figure 7 shows the shifts of the blue and red peaks, as well as the central absorption, in comparison to the variation of the average peak separation Δ_{peak} . The red peak changes consistently with absorption, but the change in the blue peak is significantly different at phase 0.049. Variations in the emission lines of Algol binaries typically occur around phase 0.0 when the secondary star eclipses the disk rotating with the primary star. This is most obvious in totally eclipsing systems. The H_α profile for phase 0.049 (post eclipse) in Figure 6 resembles a disk system during its egress phase interval, similar to TT Hya (Miller et al. 2007) or AU Mon (Atwood-Stone et al. 2012). At phase 0.66, the gas stream approaches the observer. If its material emits in H_α , it could contribute to the disk emission. Phases around 0.2 show comparable intensity in the blue-red emission peaks, while the blue emissions are stronger following the secondary eclipse. During phase 0.5-0.6, the blue emission is stronger than the red emission. Additionally, the central absorption deepens when leaving the secondary eclipse. Studies (Miller et al. 2007; Atwood-Stone et al. 2012) on accretion disks suggest that

⁴ B/R , historically known as V/R , is still widely used.

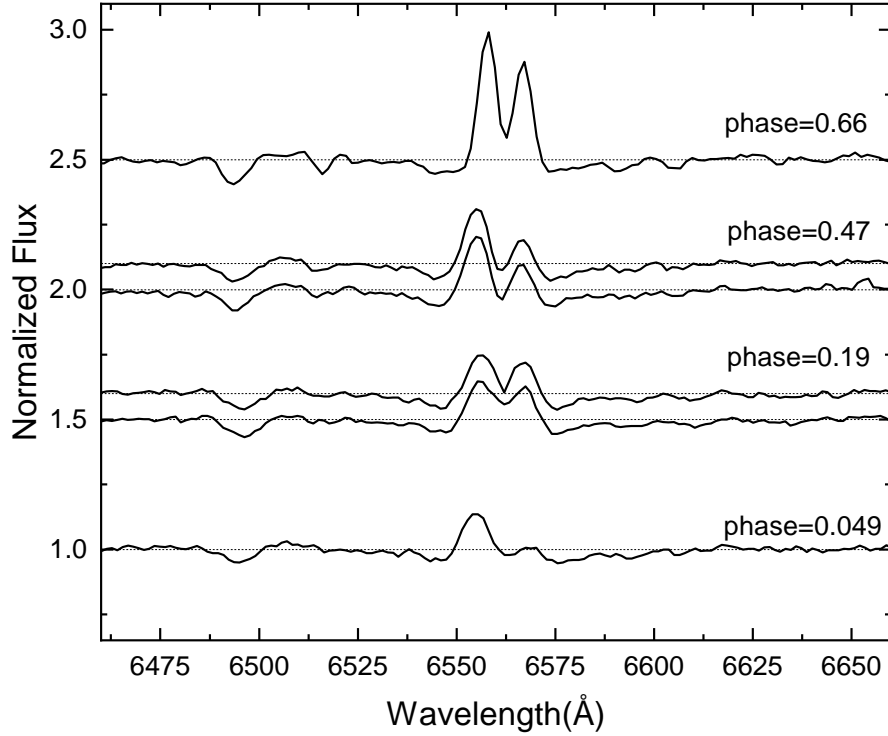


Figure 6. All the spectra show H_α profile. Fluxes are normalized to the continuum and heliocentric corrections have been applied.

this is due to the extra absorption of the secondary’s light in the reappearing part of the disk and the eclipse of the secondary star.

The direction of mass transfer is discovered to be consistent with the period change analyzed by the O-C method. We have collected all eclipse times for V583 Lyr, consisting of the new data from *Kepler* and *TESS* photometry, which are listed in Table A1 in the Appendix. The upward O-C curve in Figure 8 indicates that V583 Lyr is currently experiencing an increase in the orbital period due to mass transfer from a low-mass donor to a more massive gainer:

$$O - C = 5.064 \times 10^{-8} (\pm 0.5 \times 10^{-8}) \times E^2 - 2.1 \times 10^{-5} (\pm 1.1 \times 10^{-5}) \times E + 0.100 (\pm 0.007). \quad (4.1)$$

where E represents the epochs of the primary minima in cycles. The rate of mass transfer is estimated by assuming conservative mass transfer⁵, and the rate of period change is calculated from $\frac{\dot{P}}{P}$:

$$\frac{\dot{P}}{P} = 5.064 \times 10^{-8} \times 2 \times 365.24219 / (11.2580)^2 = 2.9 \times 10^{-7} d \cdot yr^{-1}, \quad (4.2)$$

and for the conservative mass transfer:

$$\frac{\dot{P}}{P} = \frac{3\dot{M}_1(M_1 - M_2)}{M_1M_2} \quad (4.3)$$

So the matter accreted by the primary star is calculated to be a rate at $\dot{M}_1 = 3.384 \times 10^{-8} M_\odot \cdot yr^{-1}$.

⁵ The mass transfer may not be conservative due to the system’s uncertain location in the r-q diagram. However, for estimation purposes, a conservative approach can be assumed since the accurate determination of the systemic mass loss rate is currently uncertain. Where the r-q diagram for interacting binaries shows the fractional radius of the mass gainer (R/a) plotted against the mass ratio ($q = M_2/M_1$). According to Peters & Gayley (2022), the r-q diagram can help determine whether the gas stream has a direct or tangential impact, or misses the mass gainer to form an accretion disk.

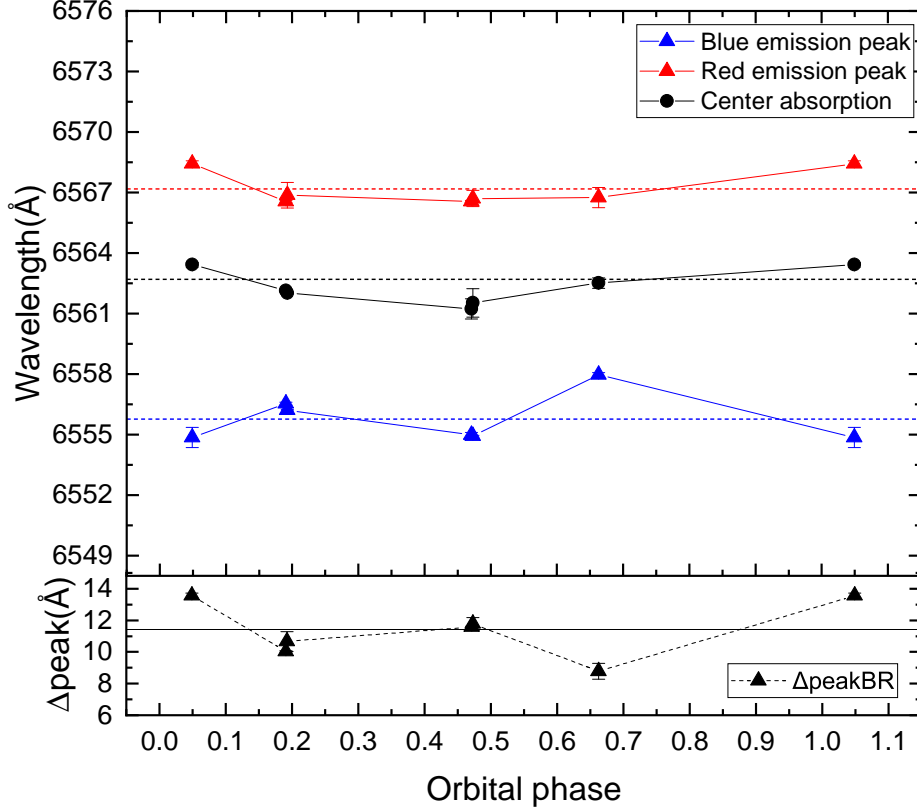


Figure 7. The shifts of the double peaks and the central absorption are plotted against the variation of the average peak separation.

Table 6. The properties of H_α emission profile. The center wavelength $B(\text{center})$, $R(\text{center})$, and $C(\text{center})$ H_α emission profile, the intensities of the blue and red emission peaks normalized to the underlying continuum I_B/I_{cont} and I_R/I_{cont} , the intensity of the central absorption I_C/I_{cont} , peak separation Δpeak_{BR} , and intensity ratio of the emission peaks B/R .

Phase	Instrument	$B(\text{center})$ (Å)	I_B/I_{cont}	$R(\text{center})$ (Å)	I_R/I_{cont}	$C(\text{center})$ (Å)	I_C/I_{cont}	Δpeak_{BR} (Å)	B/R
0.04906	BFOSC	6554.85 ± 0.5	1.13	6568.42 ± 0.15	1.01	6563.42 ± 0.12	0.99	13.57 ± 0.15	1.13
0.19080	BFOSC	6556.53 ± 0.07	1.14	6566.56 ± 0.05	1.13	6562.14 ± 0.08	1.06	10.03 ± 0.05	1.02
0.19266	BFOSC	6556.21 ± 0.04	1.15	6566.87 ± 0.63	1.12	6562.01 ± 0.03	1.01	10.66 ± 0.63	1.03
0.47104	BFOSC	6554.98 ± 0.13	1.20	6566.56 ± 0.05	1.09	6561.23 ± 0.50	0.96	11.58 ± 0.05	1.10
0.47289	BFOSC	6554.92 ± 0.05	1.21	6566.7 ± 0.4	1.09	6561.53 ± 0.70	0.98	11.78 ± 0.4	1.11
0.66266	LAMOST	6557.97 ± 0.11	1.48	6566.75 ± 0.5	1.36	6562.51 ± 0.26	1.09	8.78 ± 0.5	1.09

3.5. Pulsation analysis

The frequency analysis of V583 Lyr was conducted using the long cadence (LC) data from *Kepler* quarters 0 to 17 with Period04 (Lenz & Breger 2004). The LC observations were obtained over a continuous run of about 4 years (1,470 days) and covered nearly 130 full orbital cycles. The g-mode pulsations were initially deduced based on the range of frequencies and the mass of the primary star estimated in Section 3.3. The features of combination and group frequencies can be used to identify g mode pulsations, which can have so small frequency separations that data sets of

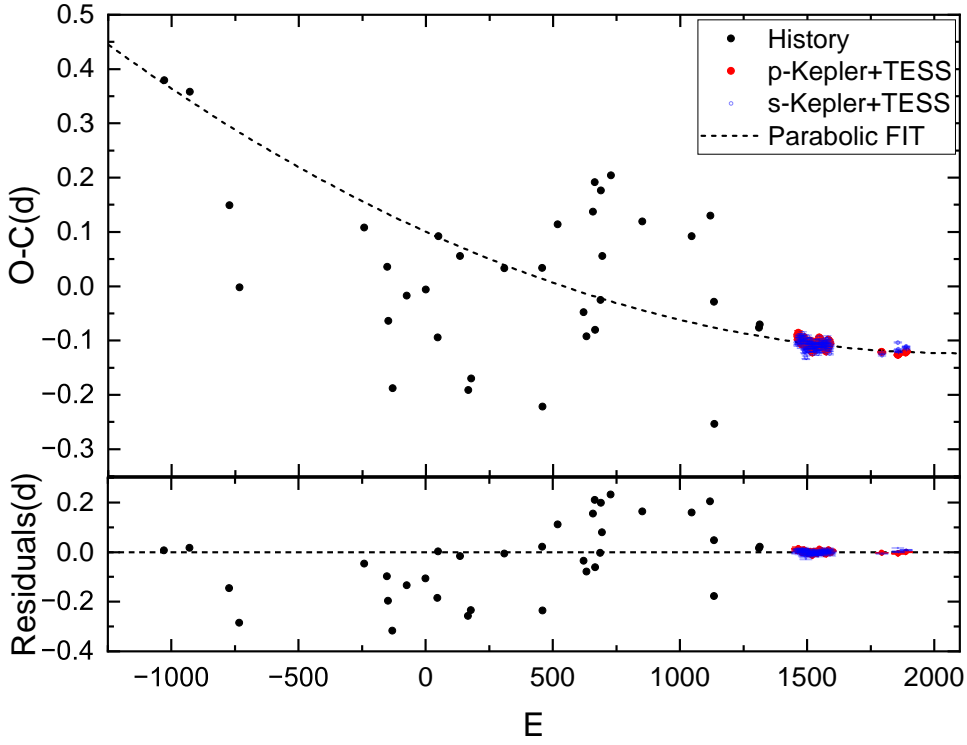


Figure 8. The theoretical fit to the O-C data for V583 Lyr. The top panel shows the parabolic fit (dashed line), and the bottom panel shows the residuals from the fit.

less than 1 year may not be able to distinguish individual pulsation frequencies. Examples of this can be found in the γ Dor- δ Sct stars KIC 11145123 (Kurtz et al. 2014; Van Reeth et al. 2015) and KIC 9244992 (Kurtz et al. 2014), as well as in the catalog of γ Dor stars presented by Li et al. (2020). Therefore, the *Kepler* LC data set, which is more credible than the short cadence (SC) data for understanding the g mode pulsation, was chosen in this work.

To disentangle the eclipse and pulsation in V583 Lyr, we use the methods from our early work on RZ Hor (Zhang et al. 2023). The frequency resolution was calculated as $\delta f_{LC} = \frac{1.5}{\Delta T} \approx 0.001 d^{-1}$, and the Nyquist frequency is $f_{Ny} = 24.464 d^{-1}$, where ΔT represents the length of the observation time. The signal-to-noise ratio (SNR) threshold for frequencies given against *Kepler* photometric data is $S/N_{Kepler} = 5.4$ (Baran et al. 2015). To compare the periodogram of the *Kepler* (SC and LC data) and *TESS* observations, we plot them together in Figure 9. The three data sets show close agreement for the four major frequencies marked with arrows. The pulsation frequencies are concentrated in the low-frequency region ($f < 9 d^{-1}$).

Combination frequencies in γ Dor and SPB stars have been widely acknowledged. According to Kurtz et al. (2015), the complex variability of dozens or hundreds of frequencies can be explained by a few base frequencies and their combination frequencies. We attempt to identify the base frequencies in the Fourier periodogram to generate the predicted frequencies. The frequency spacings are initially calculated to find the tidal splitting and equal separations. The combination frequencies are then determined based on the difference between the detected and predicted frequency, if the difference is below the δf_{LC} , the signal will be considered as combination frequency. After subtracting all the harmonic frequencies of the binary orbital period, there are 26 identified frequencies. The combination frequencies identified in Table 7 are labeled into four groups, as shown in Figure 9. We finally extracted 9 base frequencies, and 17 combination frequencies, the method used to determine frequency, amplitude, and phase errors was established by Montgomery & O’Donoghue (1999). Figure 10 shows the fitted pulsation light curve for the residuals of *Kepler* LC data with all detected frequencies.

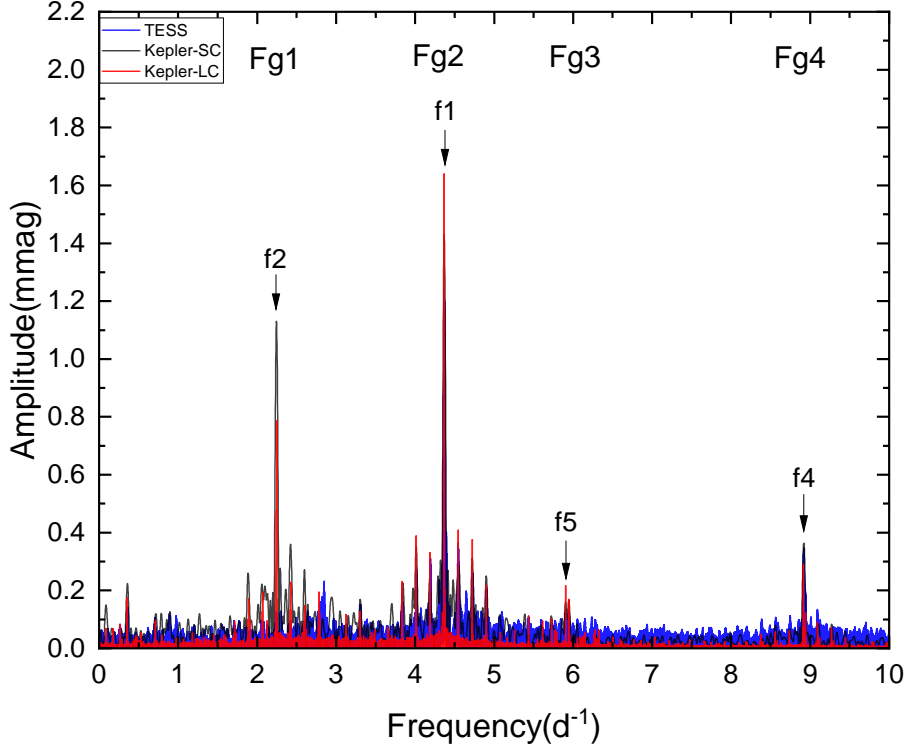


Figure 9. Comparison of the Fourier periodograms of the *TESS* (blue) and *Kepler* -SC (black), -LC (red) light curves of V583 Lyr. There are no pulsations at higher frequencies up to the Nyquist frequency. The frequency groups are labeled as four groups with Fg1, Fg2, etc.

Mode identification is based on the rotational splitting constraints of the g mode. To ensure certainty in identification, the spacings between and within multiplets must conform to the theory's demands. Dziembowski & Goode (1992) derived an approximate expression for the rotational splitting (δf_l) and rotational period (P_{rot}) for g modes. The g -mode rotational splitting characteristics are used to identify pulsation modes. Table 8 displays the g -mode rotational splitting for $l = 1$, $l = 2$, where l is the angular degree of the oscillation, m is the azimuthal quantum number. The l and m values listed in Table 8 were identified by spacing constraints. The observed rotational splitting demonstrates close agreement with theoretical predictions, thereby providing additional support for the validity of the l values. The frequency intervals $\delta f_{l=1} \approx 0.1863 d^{-1}$, $\delta f_{l=2} \approx 0.3477 d^{-1}$ correspond to the g -mode splitting ratio $R_{1,2} = \delta f_{l=1} : \delta f_{l=2} = 0.5358$, which is within a few percent of its asymptotic value $\frac{1}{\sqrt{3}}$ (Winget et al. 1991). The rotation period of the pulsating component is estimated as $P_{rot1} = \frac{1-[l(l+1)]^{-1}}{\delta f_l} \approx 2.551 d$. We have also identified additional sets of frequencies that have the same ratio of frequency spacings. Based on this, we try to speculate on their possible values of l , as indicated in Table 8. For further determination of the gainer rotation, we use the photometric method with the W-D model. The rotation of the gainer can be estimated from the photometric solutions of the mean gainer rotation factor $F_{rot1} = \frac{v_{equatorial}}{v_{synchronous}}$, which is defined as the ratio of equatorial and synchronous velocity. For a set of assigned gainer rotation factors F_{rot1} , we ran two groups of W-D models on the *TESS* and *Kepler* light curves. Figure 11 shows the results of Residuals- F_{rot1} , the minimum fall between 4.7 and 5.3. The optimal value for F_{rot1} with the least residuals is $F_{rot1} = 4.8$, supporting nearly uniform gainer rotation in V583 Lyr from accreted angular momentum. The photometric solution is used to compute the $P_{rot1} \approx 2.3454 d$, which is close to the rotation period calculated from the g -mode splitting. The apparent g -mode pulsations and the implied A spectral class for the mass-accreting primary suggest that the system may belong to a class of Algols known as oscillating EA or "oEA", such as AS Eri (Mkrtychian et al. 2004), for which the primary is a δ Scuti star. The pulsations could enhance systemic mass loss.

Table 7. The group frequencies of V583 Lyr. There are 26 identified frequencies, including 9 base frequencies, and 17 combination frequencies. The zero-point of the time-scale is 2454953.54.

Combination	Frequency (d^{-1})	Amplitude (mmag)	Phase ($rad/2\pi$)	SNR
Fg1				
F42=7f22-12f1+4f4	1.4513276(299)	0.047(4)	0.715(13)	5.8
f14=6f5+8f4-24f1	1.908725(17)	0.083(4)	0.189(7)	8.6
f24=f1-f2	2.122902(19)	0.073(4)	0.586(8)	6.8
f12=f1-f3	2.123993(18)	0.078(4)	0.045(8)	7.2
f3	2.245163(4)	0.328(4)	0.180(2)	29.3
f2	2.246230(2)	0.684(4)	0.649(1)	61.6
f11	2.421866(15)	0.090(4)	0.060(7)	7.9
f20=4f11-2f3-f22	2.595199(20)	0.070(4)	0.611(8)	6.1
f21=2f11-f3	2.598640(20)	0.070(4)	0.832(8)	6
f22	2.602494(25)	0.057(4)	0.420(11)	5.8
F27=2f22-2f11+f3	2.6071137(226)	0.062(4)	0.747(10)	5.4
f7=2f19-f5	2.781264(8)	0.170(4)	0.715(3)	15.3
f9	2.790929(12)	0.114(4)	0.785(5)	10.2
Fg2				
f18=3f1-f4	4.191528(17)	0.082(4)	0.609(7)	8.4
f43=5f1-4f2-3f4	4.300665(30)	0.047(4)	0.174(13)	5.6
f19	4.344419(19)	0.074(4)	0.826(8)	8
F13=3f9+6f3-f1	4.3663826(156)	0.09(4)	0.128(7)	9.6
f1	4.369135(1)	1.489(4)	0.577(0)	160.5
f16=6f1-3f9-6f3	4.371668(21)	0.067(4)	0.704(9)	7.3
f15=2f1-f19	4.393832(17)	0.080(4)	0.753(7)	8.8
Fg3				
f5	5.906773(72)	0.194(4)	0.615(3)	42.9
f8=2f1-f9	5.947306(8)	0.164(4)	0.247(4)	36.7
f47=2f1-2f19+f5	5.957014(32)	0.043(4)	0.218(14)	9.6
Fg4				
f33=2f1	8.738301(26)	0.054(4)	0.084(11)	19.3
f4	8.915919(5)	0.278(4)	0.947(2)	102.1
f10=15f1+f9-f5-6f4	8.940641(13)	0.107(4)	0.510(6)	39.4

Table 8. Possible rotational splittings. δf is the frequency spacing in d^{-1} . The l and m values were identified by spacing constraints. The "-" sign is for modes which have not been determined.

Label	ID	Frequency (d^{-1})	δf (d^{-1})	l	m
1	f20	2.595197	0.195733	1	0
	f9	2.790930		1	1
2	f3	2.245162	0.176784	1	-1
	f11	2.421871		1	0
	f21	2.598655		1	1
3	f2	2.246233	0.347755	2	0
	f23	2.593988		2	1
4	f9	2.790930	1.578205	1	-
	f1	4.369135		1	-
	f8	5.947306			
5	f9	2.790930	1.579225	1	-
	f44	4.370156		1	-
6	f47	5.957014	2.958905	2	-
	f4	8.915919		2	-

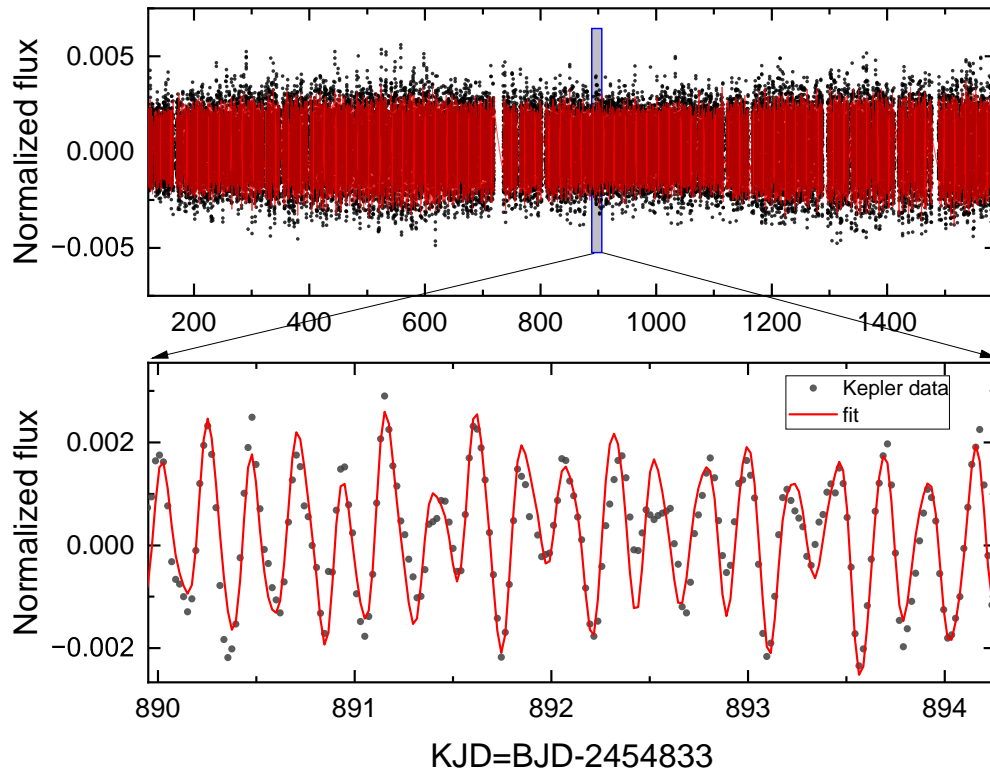


Figure 10. Multi-frequency fit for V583 Lyr. The residuals after subtracting the eclipses in the *Kepler* (LC) observations and the synthetic curve. The lower panel presents a portion of the residuals denoted with the inset box in the upper panel. The red line indicates the synthetic curve computed using all the frequencies detected.

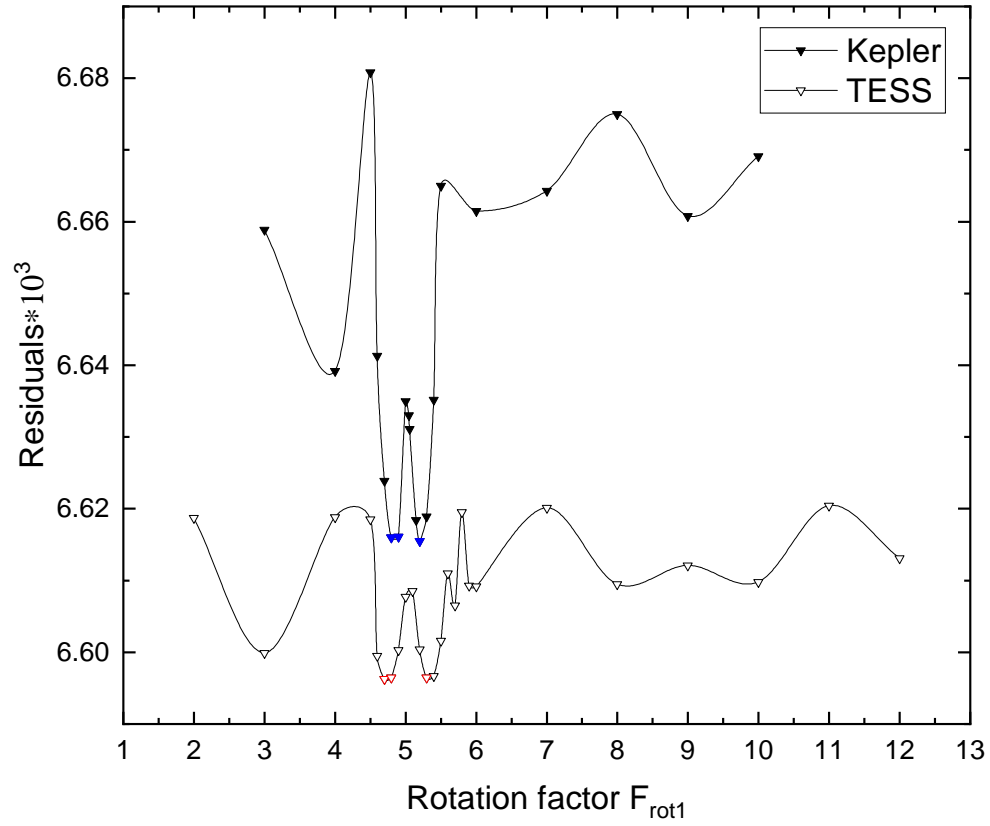


Figure 11. Results for a set of assigned gainer rotation parameters F_{rot1} modeled from *TESS* and *Kepler* photometry. All minima fall between 4.7 and 5.3, and the best $F_{rot1} = 4.8$, implying essentially uniform gainer rotation.

4. CONCLUSION AND DISCUSSION

This paper focuses on the detailed analyses of V583 Lyr, an eclipsing binary observed by the *Kepler* mission. New photometric data from *TESS*, together with *Kepler* observations, constrain a very low mass ratio for the system ($q = 0.1 \pm 0.004$). Our photometric analysis yielded results for the mass ratio q , orbital inclination i , and the relative parameters listed in Table 3, which align with the conclusions presented in Zhang et al. (2020). The ground-based spectroscopic observations, in conjunction with the results derived from *Gaia*'s BP/RP spectra, permitted the estimation of the hotter star's temperature. According to Harmanec (1988), the effective temperature of 9000 K, determined by spectral modeling, may be underestimated if the star has a mass of $3.56 M_{\odot}$. It is possible that due to the mass transfer the primary star is surrounded by stellar matter or an accretion disk. If a lower T_{eff} is adopted for B-type stars, the log g values derived from the Balmer line widths will be too small. Consequently, the secondary effective temperature (T_{eff2}) and the luminosity of the stars, $L = 4\pi R^2 \sigma T_{eff}^4$, modeled by the W-D program might be underestimated for a given T_{eff1} . Future observations and studies on V583 Lyr may allow for a more precise determination of the effective temperature, further confirming the classification of the pulsating primary star. Based on the effective temperature range of SPBs proposed by Shi et al. (2023), if the pulsating primary has a higher T_{eff1} , it could be classified as an SPB star. New spectroscopic observations of V583 Lyr were conducted in specific orbital phases, providing additional data for the construction of the Radial velocity curve. The radial velocity curve of the secondary component has facilitated the most accurate photometric modeling to date, resulting in the derivation of the absolute parameters of both components. Based on our radial velocity analysis, we determined that the orbit is circular and the half amplitude is $K_2 = 135.5 \pm 6.0 \text{ km s}^{-1}$. In addition, the system velocity is $\gamma = 53.7 \pm 3 \text{ km s}^{-1}$. It was found that the mass of the primary component is $M_1 \approx 3.56 M_{\odot}$, therefore the M_2 is calculated as $q \cdot M_2 \approx 0.36 M_{\odot}$.

V583 Lyr is discovered to be an Algol-type eclipsing binary with a gainer surrounded by an accretion disk. We examined the double-peaked emission in H_{α} lines. The variation of the double-peaked emission was explained based on the spectroscopic observations. We also gave the argument of the mass transfer by considering the O-C analysis on the orbital period, from which the matter accretion is estimated to be a rate at $\dot{M}_1 = 3.384 \times 10^{-8} M_{\odot} \cdot \text{yr}^{-1}$. The direction of mass transfer in V583 Lyr has been confirmed to be from the low-mass, filled secondary star to the massive primary star via an accretion disk. Based on our determination that the size of the gainer is $R_1/a \approx 0.074$, which falls below the ω_{min} curve identified by Lubow & Shu (1975), a stable accretion disk is confirmed in V583 Lyr. The properties of V583 Lyr are similar to those of the well-studied system TT Hya (van Hamme & Wilson 1993; Miller et al. 2007), whose $R_1/a = 0.086$ and $q = 0.226$.

We report the first detection of pulsations in V583 Lyr. The primary component of the system was found to be a g -mode pulsating star. Pulsation in V583 Lyr is detected in low frequencies, all the 26 detected frequencies are extracted lower than 9 d^{-1} . The frequency groups are predominantly composed of a few fundamental frequencies combined together, and we interpret these fundamental frequencies as originating from a small set of g modes. The frequency groups appear in the g -mode pulsators such as SPBs and γ Dor stars (McNamara et al. 2012; Kurtz et al. 2015). This observational result greatly simplifies the study of g -mode pulsations. Mode identification is based on the rotational splitting properties of the g mode. We have identified the g -mode rotational splitting of $l = 1$, $l = 2$. Their rotational splitting ratio is in close agreement with theoretical predictions, which reinforces the validity of the l values. The rotation period was estimated as $P_{orb} \approx 2.551 \text{ d}$, which was also checked by the photometric method of binary modeling. The fitting of the *TESS* and *Kepler* data results in a consistent range of optimal solutions for the F_{rot1} (see Figure 11). The optimal value for F_{rot1} with the least residuals is $F_{rot1} = 4.8$. This value aligns with the findings obtained from frequency analysis. The differential rotation can be explained by the mass accretion and the non-conservative angular momentum evolution (Derviřođlu et al. 2010).

5. ACKNOWLEDGMENTS

The research presented here is supported by the National Key R&D Program of China (grant No:2022YFE0116800), the National Natural Science Foundation of China (No. 11933008), the Young Talent Project of "Yunnan Revitalization Talent Support Program" in Yunnan Province, and the basic research project of Yunnan Province (Grant No. 202201AT070092). The photometric data used in this paper were obtained from the *Kepler* mission and the *TESS* mission, obtained from the MAST data archive at the Space Telescope Science Institute (STScI). Funding for the *TESS* mission is provided by the NASA Explorer Program. The spectral data were observed by the *LAMOST* telescope and the 2.16 m telescope at Xinglong Station, National Astronomical Observatories. The Guoshoujing Telescope (the Large Sky Area Multi-Object Fiber Spectroscopic Telescope *LAMOST*) is a national major scientific project built

by the Chinese Academy of Sciences. The project was funded by the National Development and Reform Commission. *LAMOST* is operated and managed by the National Astronomical Observatories, Chinese Academy of Sciences. Funding for the *Kepler* mission is provided by the NASA Science Mission Directorate. We acknowledge the assistance of the Xinglong 2.16 m Telescope staff. This work was supported in part by the Open Project Program of the Key Laboratory of Optical Astronomy, National Astronomical Observatories, Chinese Academy of Sciences.

APPENDIX

A. APPENDIX INFORMATION

All the eclipse times of V583 Lyr are provided in a machine readable format in Table A1.

Table A1. All the eclipse times of V583 Lyr. “p/s” means the primary minima or secondary minima.

Eclipse Times BJD–2400000	Errors (d)	p/s	Method	Observer
26919.59	-	p	pg	Guilbaut Peter
28056.617	-	p	pg	Guilbaut Peter
29812.64	-	p	pg	Guilbaut Peter
30251.547	-	p	pg	Guilbaut Peter
35779.286	-	p	pg	Berthold Thomas
36792.425	-	p	pg	Berthold Thomas
36837.357	-	p	pg	Berthold Thomas
37028.617	-	p	pg	Berthold Thomas
37659.23	-	p	pg	Berthold Thomas
38503.584	-	p	pg	Berthold Thomas
39021.359	-	p	pg	Berthold Thomas
39055.319	-	p	pg	Berthold Thomas
40023.462	-	p	pg	Berthold Thomas
40383.468	-	p	pg	Berthold Thomas
40507.326	-	p	pg	Berthold Thomas
41982.314	-	p	pg	Berthold Thomas
43659.742	-	p	pg	Guilbaut Peter
43670.744	-	p	pg	Guilbaut Peter
44346.554	-	p	pg	Berthold Thomas
45089.755	-	p	pg	Guilbaut Peter
45494.698	-	p	pg	Guilbaut Peter
45618.49	-	p	pg	Guilbaut Peter
45911.425	-	p	pg	Berthold Thomas
45990.285	-	p	pg	Berthold Thomas
46001.271	-	p	pg	Berthold Thomas
46237.742	-	p	pg	Guilbaut Peter
46260.459	-	p	pg	Berthold Thomas
46316.628	-	p	pg	Guilbaut Peter
46699.545	-	p	pg	Guilbaut Peter
46733.468	-	p	pg	Guilbaut Peter

Eclipse times of V583 Lyr(continue)

Eclipse Times BJD-2400000	error (d)	p/s	Method	Observer
48095.44	-	p	pg	Berthold Thomas
50279.445	-	p	pg	Berthold Thomas
51101.31	-	p	pg	Dahlmark L
51275.424	-	s	ccd	Paschke Anton
51270.02	-	p	-	ROTSE
53262.62	-	p	-	Krajci estimate
53296.4	-	p	-	Krajci estimate
54962.54906	0.00118	p	ccd	Kepler
54973.80475	0.00495	p	ccd	Kepler
54985.06057	0.00503	p	ccd	Kepler
54996.32747	0.00398	p	ccd	Kepler
55007.58176	0.00346	p	ccd	Kepler
55018.83729	0.00216	p	ccd	Kepler
55030.09478	0.00224	p	ccd	Kepler
55041.34874	0.00305	p	ccd	Kepler
55052.60903	0.00176	p	ccd	Kepler
55075.12352	0.00109	p	ccd	Kepler
55086.37657	0.00091	p	ccd	Kepler
55097.63569	0.00102	p	ccd	Kepler
55108.8938	0.00084	p	ccd	Kepler
55120.15145	0.00131	p	ccd	Kepler
55131.40105	0.00113	p	ccd	Kepler
55142.66566	0.00117	p	ccd	Kepler
55153.92044	0.00053	p	ccd	Kepler
55165.1765	0.00077	p	ccd	Kepler
55176.4326	0.00177	p	ccd	Kepler
55187.69212	0.00109	p	ccd	Kepler
55198.95328	0.00073	p	ccd	Kepler
55210.21672	0.00114	p	ccd	Kepler
55221.46412	0.001	p	ccd	Kepler
55243.98384	0.00114	p	ccd	Kepler
55255.25143	0.00162	p	ccd	Kepler
55266.50145	0.00106	p	ccd	Kepler
55277.76019	0.00128	p	ccd	Kepler
55289.01458	0.00101	p	ccd	Kepler
55300.27322	0.00099	p	ccd	Kepler
55311.53429	0.0009	p	ccd	Kepler
55322.79061	0.00115	p	ccd	Kepler
55334.052	0.00092	p	ccd	Kepler
55345.30826	0.00079	p	ccd	Kepler
55356.56225	0.00059	p	ccd	Kepler
55367.82196	0.00152	p	ccd	Kepler
55379.07842	0.00252	p	ccd	Kepler
55390.33124	0.00058	p	ccd	Kepler

Eclipse times of V583 Lyr(continue)

Eclipse Times BJD-2400000	error (d)	p/s	Method	Observer
55401.58704	0.0017	p	ccd	Kepler
55412.84894	0.00117	p	ccd	Kepler
55424.10409	0.00154	p	ccd	Kepler
55435.36015	0.00095	p	ccd	Kepler
55446.62026	0.00119	p	ccd	Kepler
55457.88401	0.00063	p	ccd	Kepler
55469.13395	0.00118	p	ccd	Kepler
55480.39487	0.00066	p	ccd	Kepler
55491.64639	0.00106	p	ccd	Kepler
55502.91536	0.00077	p	ccd	Kepler
55514.17041	0.00089	p	ccd	Kepler
55525.4341	0.00077	p	ccd	Kepler
55536.68032	0.00092	p	ccd	Kepler
55547.93501	0.00098	p	ccd	Kepler
55570.45358	0.00072	p	ccd	Kepler
55581.7068	0.00068	p	ccd	Kepler
55592.97095	0.00155	p	ccd	Kepler
55604.22349	0.00069	p	ccd	Kepler
55615.47533	0.00109	p	ccd	Kepler
55626.74445	0.00092	p	ccd	Kepler
55649.26482	0.00105	p	ccd	Kepler
55660.51934	0.00147	p	ccd	Kepler
55671.78466	0.00132	p	ccd	Kepler
55683.04284	0.00104	p	ccd	Kepler
55694.29844	0.00074	p	ccd	Kepler
55705.55047	0.001	p	ccd	Kepler
55716.80923	0.00081	p	ccd	Kepler
55728.06454	0.0012	p	ccd	Kepler
55750.58122	0.00065	p	ccd	Kepler
55761.84343	0.00087	p	ccd	Kepler
55773.09822	0.00074	p	ccd	Kepler
55784.35277	0.00072	p	ccd	Kepler
55795.60865	0.00075	p	ccd	Kepler
55806.86645	0.00236	p	ccd	Kepler
55818.13032	0.00082	p	ccd	Kepler
55829.39502	0.00121	p	ccd	Kepler
55840.64421	0.00122	p	ccd	Kepler
55851.90991	0.00188	p	ccd	Kepler
55863.16541	0.00061	p	ccd	Kepler
55874.42462	0.00103	p	ccd	Kepler
55885.68001	0.00071	p	ccd	Kepler
55908.19435	0.00057	p	ccd	Kepler
55919.46203	0.00148	p	ccd	Kepler
55930.72482	0.0012	p	ccd	Kepler

Eclipse times of V583 Lyr(continue)

Eclipse Times BJD-2400000	error (d)	p/s	Method	Observer
55941.97944	0.00058	p	ccd	Kepler
55953.23899	0.00097	p	ccd	Kepler
55964.49227	0.00105	p	ccd	Kepler
55975.74501	0.00084	p	ccd	Kepler
55998.26247	0.00083	p	ccd	Kepler
56009.52291	0.00096	p	ccd	Kepler
56020.78218	0.00113	p	ccd	Kepler
56032.03649	0.0004	p	ccd	Kepler
56043.29263	0.0017	p	ccd	Kepler
56054.54715	0.00095	p	ccd	Kepler
56065.80598	0.00192	p	ccd	Kepler
56077.06137	0.00097	p	ccd	Kepler
56088.32463	0.00085	p	ccd	Kepler
56099.57735	0.00102	p	ccd	Kepler
56110.83719	0.00112	p	ccd	Kepler
56122.09666	0.00096	p	ccd	Kepler
56133.34666	0.00062	p	ccd	Kepler
56144.60422	0.00096	p	ccd	Kepler
56155.86245	0.00471	p	ccd	Kepler
56167.11712	0.00063	p	ccd	Kepler
56178.37765	0.00087	p	ccd	Kepler
56189.63674	0.00114	p	ccd	Kepler
56200.89507	0.00043	p	ccd	Kepler
56212.15494	0.00137	p	ccd	Kepler
56223.40392	0.00059	p	ccd	Kepler
56234.67182	0.0007	p	ccd	Kepler
56245.79806	0.00968	p	ccd	Kepler
56257.18703	0.00069	p	ccd	Kepler
56279.69705	0.00116	p	ccd	Kepler
56290.96701	0.00087	p	ccd	Kepler
56302.2212	0.00109	p	ccd	Kepler
56324.74697	0.00132	p	ccd	Kepler
56335.99261	0.00128	p	ccd	Kepler
56347.26161	0.00143	p	ccd	Kepler
56369.77672	0.00121	p	ccd	Kepler
56381.02833	0.00079	p	ccd	Kepler
56392.36089	0.00757	p	ccd	Kepler
56403.54591	0.00132	p	ccd	Kepler
58688.88345	0.00103	p	ccd	TESS
58700.14082	0.00103	p	ccd	TESS
59398.12574	0.001	p	ccd	TESS
59409.38417	0.00099	p	ccd	TESS
59420.64174	0.00101	p	ccd	TESS
59431.90059	0.00101	p	ccd	TESS

Eclipse times of V583 Lyr(continue)

Eclipse Times BJD-2400000	error (d)	p/s	Method	Observer
59443.1592	0.00101	p	ccd	TESS
59747.12617	0.00099	p	ccd	TESS
59758.38281	0.00097	p	ccd	TESS
59780.90062	0.00101	p	ccd	TESS
59792.15818	0.00098	p	ccd	TESS
54956.90505	0.00281	s	ccd	Kepler
54968.16029	0.00203	s	ccd	Kepler
54979.4222	0.00226	s	ccd	Kepler
54990.68071	0.00284	s	ccd	Kepler
55013.19861	0.0025	s	ccd	Kepler
55024.46451	0.00175	s	ccd	Kepler
55035.72404	0.00226	s	ccd	Kepler
55046.97638	0.00348	s	ccd	Kepler
55058.23075	0.00284	s	ccd	Kepler
55069.497	0.00201	s	ccd	Kepler
55080.75517	0.00334	s	ccd	Kepler
55103.27367	0.00235	s	ccd	Kepler
55114.51521	0.00833	s	ccd	Kepler
55125.77682	0.00335	s	ccd	Kepler
55137.03481	0.00261	s	ccd	Kepler
55148.30066	0.0025	s	ccd	Kepler
55159.56326	0.00236	s	ccd	Kepler
55170.80649	0.0032	s	ccd	Kepler
55182.08216	0.00297	s	ccd	Kepler
55193.33279	0.0032	s	ccd	Kepler
55204.58318	0.00368	s	ccd	Kepler
55215.83515	0.00245	s	ccd	Kepler
55227.10101	0.00183	s	ccd	Kepler
55238.36215	0.00416	s	ccd	Kepler
55249.61753	0.00366	s	ccd	Kepler
55260.85453	0.00252	s	ccd	Kepler
55272.13018	0.00282	s	ccd	Kepler
55283.36942	0.00412	s	ccd	Kepler
55294.63165	0.00194	s	ccd	Kepler
55305.8954	0.00234	s	ccd	Kepler
55317.13496	0.00419	s	ccd	Kepler
55328.38962	0.00337	s	ccd	Kepler
55339.66594	0.00267	s	ccd	Kepler
55350.91955	0.00323	s	ccd	Kepler
55362.17814	0.00303	s	ccd	Kepler
55373.43837	0.00264	s	ccd	Kepler
55384.70656	0.00191	s	ccd	Kepler
55395.9708	0.00228	s	ccd	Kepler
55407.20812	0.00292	s	ccd	Kepler

Eclipse times of V583 Lyr(continue)

Eclipse Times BJD-2400000	error (d)	p/s	Method	Observer
55418.49212	0.00245	s	ccd	Kepler
55429.73445	0.00303	s	ccd	Kepler
55441.00253	0.0042	s	ccd	Kepler
55452.24059	0.00297	s	ccd	Kepler
55463.51822	0.00323	s	ccd	Kepler
55474.77325	0.00434	s	ccd	Kepler
55486.0278	0.00271	s	ccd	Kepler
55497.28764	0.00211	s	ccd	Kepler
55508.54619	0.00325	s	ccd	Kepler
55519.79544	0.00309	s	ccd	Kepler
55531.05527	0.00241	s	ccd	Kepler
55542.31538	0.00276	s	ccd	Kepler
55576.09074	0.00239	s	ccd	Kepler
55587.34936	0.00261	s	ccd	Kepler
55598.60432	0.00391	s	ccd	Kepler
55609.8563	0.00255	s	ccd	Kepler
55621.11857	0.00226	s	ccd	Kepler
55632.37231	0.00291	s	ccd	Kepler
55643.61911	0.003	s	ccd	Kepler
55654.88322	0.00233	s	ccd	Kepler
55666.14079	0.00353	s	ccd	Kepler
55677.40812	0.00312	s	ccd	Kepler
55688.65996	0.00283	s	ccd	Kepler
55699.92197	0.00268	s	ccd	Kepler
55711.17194	0.003	s	ccd	Kepler
55722.42968	0.00292	s	ccd	Kepler
55733.69563	0.00298	s	ccd	Kepler
55744.96258	0.00268	s	ccd	Kepler
55756.21379	0.00245	s	ccd	Kepler
55767.4725	0.00238	s	ccd	Kepler
55778.72901	0.00301	s	ccd	Kepler
55789.98065	0.00268	s	ccd	Kepler
55801.23973	0.00263	s	ccd	Kepler
55812.49611	0.003	s	ccd	Kepler
55823.75901	0.0029	s	ccd	Kepler
55835.0063	0.00223	s	ccd	Kepler
55846.26431	0.00238	s	ccd	Kepler
55857.51895	0.00312	s	ccd	Kepler
55868.78511	0.00308	s	ccd	Kepler
55880.05026	0.0027	s	ccd	Kepler
55891.31539	0.00266	s	ccd	Kepler
55902.57346	0.00372	s	ccd	Kepler
55913.82827	0.003	s	ccd	Kepler
55925.09629	0.00238	s	ccd	Kepler

Eclipse times of V583 Lyr(continue)

Eclipse Times BJD-2400000	error (d)	p/s	Method	Observer
55936.34373	0.0037	s	ccd	Kepler
55947.59831	0.00362	s	ccd	Kepler
55958.73708	0.00249	s	ccd	Kepler
55970.11253	0.0035	s	ccd	Kepler
55981.37338	0.00408	s	ccd	Kepler
55992.62052	0.00324	s	ccd	Kepler
56003.88844	0.00254	s	ccd	Kepler
56026.39139	0.00399	s	ccd	Kepler
56037.6573	0.00242	s	ccd	Kepler
56048.91687	0.00539	s	ccd	Kepler
56060.17711	0.00342	s	ccd	Kepler
56071.42991	0.00329	s	ccd	Kepler
56082.69783	0.00263	s	ccd	Kepler
56093.95032	0.0034	s	ccd	Kepler
56105.21256	0.00465	s	ccd	Kepler
56116.46626	0.00242	s	ccd	Kepler
56150.23627	0.00379	s	ccd	Kepler
56161.49621	0.00263	s	ccd	Kepler
56172.75896	0.00356	s	ccd	Kepler
56184.01362	0.00292	s	ccd	Kepler
56195.27489	0.00318	s	ccd	Kepler
56217.78816	0.00444	s	ccd	Kepler
56229.03941	0.00339	s	ccd	Kepler
56240.31089	0.00244	s	ccd	Kepler
56251.59865	0.00696	s	ccd	Kepler
56262.82947	0.00344	s	ccd	Kepler
56274.0871	0.00258	s	ccd	Kepler
56285.34141	0.00259	s	ccd	Kepler
56296.60346	0.00298	s	ccd	Kepler
56307.84644	0.00249	s	ccd	Kepler
56330.37344	0.00385	s	ccd	Kepler
56341.61468	0.00425	s	ccd	Kepler
56352.87622	0.00254	s	ccd	Kepler
56364.1289	0.00308	s	ccd	Kepler
56375.39187	0.00393	s	ccd	Kepler
56386.64076	0.00329	s	ccd	Kepler
56397.91581	0.00168	s	ccd	Kepler
56409.16968	0.00302	s	ccd	Kepler
56420.42958	0.00367	s	ccd	Kepler
58694.50683	0.00128	s	ccd	TESS
58705.76915	0.00119	s	ccd	TESS
59392.50503	0.00116	s	ccd	TESS
59403.77771	0.00112	s	ccd	TESS
59415.02322	0.00086	s	ccd	TESS

Eclipse times of V583 Lyr(continue)

Eclipse Times BJD-2400000	error (d)	p/s	Method	Observer
59426.27554	0.001	s	ccd	TESS
59437.53455	0.00114	s	ccd	TESS
59752.76346	0.00109	s	ccd	TESS
59764.02365	0.00096	s	ccd	TESS
59775.27987	0.00109	s	ccd	TESS
59786.53376	0.00116	s	ccd	TESS

REFERENCES

- Aerts, C., Christensen-Dalsgaard, J., & Kurtz, D. W. 2010, *Asteroseismology*, doi: [10.1007/978-1-4020-5803-5](https://doi.org/10.1007/978-1-4020-5803-5)
- Atwood-Stone, C., Miller, B. P., Richards, M. T., Budaj, J., & Peters, G. J. 2012, *ApJ*, 760, 134, doi: [10.1088/0004-637X/760/2/134](https://doi.org/10.1088/0004-637X/760/2/134)
- Baglin, A., Breger, M., Chevalier, C., et al. 1973, *A&A*, 23, 221
- Balona, L. A., Daszyńska-Daszkiewicz, J., & Pamyatnykh, A. A. 2015, *MNRAS*, 452, 3073, doi: [10.1093/mnras/stv1513](https://doi.org/10.1093/mnras/stv1513)
- Baran, A. S., Koen, C., & Pokrzywka, B. 2015, *MNRAS*, 448, L16, doi: [10.1093/mnrasl/slu194](https://doi.org/10.1093/mnrasl/slu194)
- Ciddor, P. E. 1996, *Appl. Opt.*, 35, 1566, doi: [10.1364/AO.35.001566](https://doi.org/10.1364/AO.35.001566)
- Davenport, J. R. A. 2016, *ApJ*, 829, 23, doi: [10.3847/0004-637X/829/1/23](https://doi.org/10.3847/0004-637X/829/1/23)
- Dervişoğlu, A., Tout, C. A., & Ibanoglu, C. 2010, *MNRAS*, 406, 1071, doi: [10.1111/j.1365-2966.2010.16732.x](https://doi.org/10.1111/j.1365-2966.2010.16732.x)
- Djurašević, G., Latković, O., Vince, I., & Cséki, A. 2010, *Monthly Notices of the Royal Astronomical Society*, 409, 329, doi: [10.1111/j.1365-2966.2010.17310.x](https://doi.org/10.1111/j.1365-2966.2010.17310.x)
- Doğan, S., Nixon, C., King, A., & Price, D. J. 2015, *Monthly Notices of the Royal Astronomical Society*, 449, 1251, doi: [10.1093/mnras/stv347](https://doi.org/10.1093/mnras/stv347)
- Dziembowski, W. A., & Goode, P. R. 1992, *ApJ*, 394, 670, doi: [10.1086/171621](https://doi.org/10.1086/171621)
- Fan, Z., Wang, H., Jiang, X., et al. 2016, *PASP*, 128, 115005, doi: [10.1088/1538-3873/128/969/115005](https://doi.org/10.1088/1538-3873/128/969/115005)
- Gaia Collaboration. 2022, *VizieR Online Data Catalog*, I/355
- Gaulme, P., & Guzik, J. A. 2019, *A&A*, 630, A106, doi: [10.1051/0004-6361/201935821](https://doi.org/10.1051/0004-6361/201935821)
- Harmanec, P. 1988, *Bulletin of the Astronomical Institutes of Czechoslovakia*, 39, 329
- Kaye, A. B., Handler, G., Krisciunas, K., Poretti, E., & Zerbi, F. M. 1999, *PASP*, 111, 840, doi: [10.1086/316399](https://doi.org/10.1086/316399)
- Koch, D. G., Borucki, W. J., Basri, G., et al. 2010, *ApJL*, 713, L79, doi: [10.1088/2041-8205/713/2/L79](https://doi.org/10.1088/2041-8205/713/2/L79)
- Koleva, M., Prugniel, P., Bouchard, A., & Wu, Y. 2009, *A&A*, 501, 1269, doi: [10.1051/0004-6361/200811467](https://doi.org/10.1051/0004-6361/200811467)
- Kurtz, D. W., Saio, H., Takata, M., et al. 2014, *MNRAS*, 444, 102, doi: [10.1093/mnras/stu1329](https://doi.org/10.1093/mnras/stu1329)
- Kurtz, D. W., Shibahashi, H., Murphy, S. J., Bedding, T. R., & Bowman, D. M. 2015, *MNRAS*, 450, 3015, doi: [10.1093/mnras/stv868](https://doi.org/10.1093/mnras/stv868)
- Kurtz, M. J., Mink, D. J., Wyatt, W. F., et al. 1992, in *Astronomical Society of the Pacific Conference Series*, Vol. 25, *Astronomical Data Analysis Software and Systems I*, ed. D. M. Worrall, C. Biemesderfer, & J. Barnes, 432
- Kurucz, R. L. 1979, *ApJS*, 40, 1, doi: [10.1086/190589](https://doi.org/10.1086/190589)
- Larwood, J. D., Nelson, R. P., Papaloizou, J. C. B., & Terquem, C. 1996, *Monthly Notices of the Royal Astronomical Society*, 282, 597, doi: [10.1093/mnras/282.2.597](https://doi.org/10.1093/mnras/282.2.597)
- Lenz, P., & Breger, M. 2004, in *The A-Star Puzzle*, ed. J. Zverko, J. Ziznovsky, S. J. Adelman, & W. W. Weiss, Vol. 224, 786–790, doi: [10.1017/S1743921305009750](https://doi.org/10.1017/S1743921305009750)
- Li, G., Van Reeth, T., Bedding, T. R., et al. 2020, *MNRAS*, 491, 3586, doi: [10.1093/mnras/stz2906](https://doi.org/10.1093/mnras/stz2906)
- Lightkurve Collaboration, Cardoso, J. V. d. M., Hedges, C., et al. 2018, *Lightkurve: Kepler and TESS time series analysis in Python*, *Astrophysics Source Code Library*, record ascl:1812.013. <http://ascl.net/1812.013>
- Lorenzi, L. 1980, *A&A*, 85, 342
- Lubow, S. H., & Shu, F. H. 1975, *ApJ*, 198, 383, doi: [10.1086/153614](https://doi.org/10.1086/153614)
- Luo, A. L., Zhao, Y. H., Zhao, G., & et al. 2022, *VizieR Online Data Catalog: LAMOST DR7 catalogs (Luo+, 2019)*, *VizieR On-line Data Catalog: V/156*. Originally published in: 2019RAA.in.prep..L
- Marquardt, D. W. 1963, *Journal of the Society for Industrial and Applied Mathematics*, 11, 431, doi: [10.1137/0111030](https://doi.org/10.1137/0111030)
- McNamara, B. J., Jackiewicz, J., & McKeever, J. 2012, *AJ*, 143, 101, doi: [10.1088/0004-6256/143/4/101](https://doi.org/10.1088/0004-6256/143/4/101)
- Mennickent, R. E. 2022, *Galaxies*, 10, 15, doi: [10.3390/galaxies10010015](https://doi.org/10.3390/galaxies10010015)
- Miller, B., Budaj, J., Richards, M., Koubský, P., & Peters, G. J. 2007, *ApJ*, 656, 1075, doi: [10.1086/510476](https://doi.org/10.1086/510476)
- Mink, D. J., & Kurtz, M. J. 1998, in *Astronomical Society of the Pacific Conference Series*, Vol. 145, *Astronomical Data Analysis Software and Systems VII*, ed. R. Albrecht, R. N. Hook, & H. A. Bushouse, 93
- Mkrtychian, D. E., Kusakin, A. V., Rodriguez, E., et al. 2004, *A&A*, 419, 1015, doi: [10.1051/0004-6361:20040095](https://doi.org/10.1051/0004-6361:20040095)
- Montgomery, M. H., & O'Donoghue, D. 1999, *Delta Scuti Star Newsletter*, 13, 28
- Peters, G., & Gayley, K. 2022, in *American Astronomical Society Meeting Abstracts*, Vol. 54, *American Astronomical Society Meeting #240*, 205.08
- Peters, G. J., & Polidan, R. S. 1998, *ApJL*, 500, L17, doi: [10.1086/311398](https://doi.org/10.1086/311398)

- Prugniel, P., & Soubiran, C. 2001, *A&A*, 369, 1048, doi: [10.1051/0004-6361:20010163](https://doi.org/10.1051/0004-6361:20010163)
- Prugniel, P., Vauglin, I., & Koleva, M. 2011, *A&A*, 531, A165, doi: [10.1051/0004-6361/201116769](https://doi.org/10.1051/0004-6361/201116769)
- Prša, A., Batalha, N., Slawson, R. W., et al. 2011, *AJ*, 141, 83, doi: [10.1088/0004-6256/141/3/83](https://doi.org/10.1088/0004-6256/141/3/83)
- Richards, M. T., & Albright, G. E. 1999, *ApJS*, 123, 537, doi: [10.1086/313242](https://doi.org/10.1086/313242)
- Ricker, G. R., Winn, J. N., Vanderspek, R., et al. 2015, *Journal of Astronomical Telescopes, Instruments, and Systems*, 1, 014003, doi: [10.1117/1.JATIS.1.1.014003](https://doi.org/10.1117/1.JATIS.1.1.014003)
- Ruciński, S. M. 1969, *AcA*, 19, 245
- Sánchez-Blázquez, P., Peletier, R. F., Jiménez-Vicente, J., et al. 2006, *MNRAS*, 371, 703, doi: [10.1111/j.1365-2966.2006.10699.x](https://doi.org/10.1111/j.1365-2966.2006.10699.x)
- Shi, X.-d., Qian, S.-b., Zhu, L.-y., & Li, L.-j. 2023, *ApJS*, 268, 16, doi: [10.3847/1538-4365/ace88c](https://doi.org/10.3847/1538-4365/ace88c)
- Tonry, J., & Davis, M. 1979, *AJ*, 84, 1511, doi: [10.1086/112569](https://doi.org/10.1086/112569)
- van Hamme, W. 1993, *AJ*, 106, 2096, doi: [10.1086/116788](https://doi.org/10.1086/116788)
- van Hamme, W., & Wilson, R. E. 1993, *MNRAS*, 262, 220, doi: [10.1093/mnras/262.1.220](https://doi.org/10.1093/mnras/262.1.220)
- Van Reeth, T., Tkachenko, A., & Aerts, C. 2016, *A&A*, 593, A120, doi: [10.1051/0004-6361/201628616](https://doi.org/10.1051/0004-6361/201628616)
- Van Reeth, T., Tkachenko, A., Aerts, C., et al. 2015, *A&A*, 574, A17, doi: [10.1051/0004-6361/201424585](https://doi.org/10.1051/0004-6361/201424585)
- von Zeipel, H. 1924, *MNRAS*, 84, 665, doi: [10.1093/mnras/84.9.665](https://doi.org/10.1093/mnras/84.9.665)
- Waelkens, C. 1991, *A&A*, 246, 453
- Wilson, R. E. 1979, *ApJ*, 234, 1054, doi: [10.1086/157588](https://doi.org/10.1086/157588)
- . 1994, *PASP*, 106, 921, doi: [10.1086/133464](https://doi.org/10.1086/133464)
- Wilson, R. E., & Devinney, E. J. 1971, *ApJ*, 166, 605, doi: [10.1086/150986](https://doi.org/10.1086/150986)
- Winget, D. E., Nather, R. E., Clemens, J. C., et al. 1991, *ApJ*, 378, 326, doi: [10.1086/170434](https://doi.org/10.1086/170434)
- Zasche, P., Wolf, M., Kučáková, H., et al. 2015, *AJ*, 149, 197, doi: [10.1088/0004-6256/149/6/197](https://doi.org/10.1088/0004-6256/149/6/197)
- Zhang, H., Qian, S., & Liao, W. 2023, *PASJ*, 75, 732, doi: [10.1093/pasj/psad033](https://doi.org/10.1093/pasj/psad033)
- Zhang, J., Qian, S.-B., Han, Z.-T., & Wu, Y. 2017, *MNRAS*, 466, 1118, doi: [10.1093/mnras/stw3153](https://doi.org/10.1093/mnras/stw3153)
- Zhang, J., Qian, S.-B., & Lyu, B. 2020, *Publications of the Astronomical Society of the Pacific*, 132, 114201, doi: [10.1088/1538-3873/abacd4](https://doi.org/10.1088/1538-3873/abacd4)